APPLIED GEOPHYSICS, Vol.21, No.1 (March 2024), P. 1−16, 16 Figures.
DOI:10.1007/s11770-024-1040-8

Permeability Estimation of Shale Oil Reservoir with Laboratory-derived Data: A Case Study of the Chang 7 Member in Ordos Basin

Zhang Lin[1], Gao Li[1], Ba Jing[1]*, Zhang Meng-Bo[2], José M. Carcione[1,3], and Liu Wei-Hua[4]

Abstract: The shale oil reservoir within the Yanchang Formations of Ordos Basin harbors substantial oil and gas resources and has recently emerged as the primary focus of unconventional oil and gas exploration and development. Due to its complex pore and throat structure, pronounced heterogeneity, and tight reservoir characteristics, the techniques for conventional oil and gas exploration and production face challenges in comprehensive implementation, also indicating that as a vital parameter for evaluating the physical properties of a reservoir, permeability cannot be effectively estimated. This study selects 21 tight sandstone samples from the Q area within the shale oil formations of Ordos Basin. We systematically conduct the experiments to measure porosity, permeability, ultrasonic wave velocities, and resistivity at varying confining pressures. Results reveal that these measurements exhibit nonlinear changes in response to effective pressure. By using these experimental data and effective medium model, empirical relationships between P- and S-wave velocities, permeability and resistivity and effective pressure are established at logging and seismic scales. Furthermore, relationships between P-wave impedance and permeability, and resistivity and permeability are determined. A comparison between the predicted permeability and logging data demonstrates that the impedance–permeability relationship yields better results in contrast to those of resistivity–permeability relationship. These relationships are further applied to the seismic interpretation of shale oil reservoir in the target layer, enabling the permeability profile predictions based on inverse P-wave impedance. The predicted results are evaluated with actual production data, revealing a better agreement between predicted results and logging data and productivity.

Keywords: shale oil reservoir, P-wave impedance, resistivity, permeability, rock physics experiment

Introduction

With the growing need for oil and gas resources as a result of societal advancement and the depletion of conventional oil and gas reserves, unconventional oil and gas reservoirs have emerged as a primary area of research at the strategic level for many countries (Lai et al., 2022; Hosseiny and Mohseni, 2023). Shale oil, as a sort of unconventional hydrocarbon resources,

Manuscript received by the Editor September 22, 2023; revised manuscript received November 6, 2023
1. School of Earth Sciences and Engineering, Hohai University, Nanjing, Jiangsu, 211000.
2. Exploration and Development Research Institute of PetroChina, Changqing Oilfield Company, Xi'an Shanxi, 710018.
3. National Institute of Oceanography and Applied Geophysics (OGS), Sgonico, Trieste 34010.
4. Sinopec Geophysical Research Institute, Nanjing, Jiangsu, 211103.
* Corresponding author: Ba Jing (Email: jba@hhu.edu.cn)

is considered with abundant reserves and extensive distribution, and is potentially treated as a prospective cornerstone for future reserve growth (Liu et al., 2022; Shi et al., 2021; Zhang et al., 2023; Zhao et al., 2023). The shale oil resources of China are predominantly distributed into the Songliao, Ordos, Junggar, Qaidam, and Fushun Basins (Jia et al., 2012). The Chang 7 Member of the Ordos Basin, as the principal stratum for shale oil exploration and development, exhibits a complex pore and throat structure and substantial heterogeneity with tight rocks. These complexities lead to the significant challenges for the effective prediction and exploitation of shale oil reservoirs (Yang et al., 2013).

In recent years, many scholars have probed into the shale oil reservoir prediction methods. Guo et al. (2013) introduced the construction process of a shale rock physics model, considering mineral components and pores characterized by isotropic and preferred orientation distributions. They explored the impacts of clay particle orientation preferences on seismic properties, geomechanics, and the brittleness index. Deng et al. (2015) analyzed the microscopic pore structure of the Longmaxi Formation shale using scanning electron microscopy and computed tomography scanning imaging techniques. They proposed a seismic rock physics model combined with the acoustic wave experiments, indicating the role of skeleton composition minerals, total organic carbon content, and porosity in changing the elastic properties. Zhang et al. (2015) presented a shale rock physics model by analyzing mineral, porosity, fluid, and anisotropy features of shale formations and predicted the S-wave velocity and minimum horizontal stress of shale formation. Zhang et al. (2016) developed a rock physics model to describe the intrinsic anisotropy of shale with the Backus averaging, self-consistent, and differential effective medium models. They analyzed the influences of clay minerals, crack-like pores, kerogen and their preferred orientation on the elastic anisotropy. Tomski et al. (2022) analyzed the crucial characteristics of unconventional Bakken shale reservoirs using 3D seismic and logging data and estimated the total porosity of the formation by applying the prestack seismic inversion results. Cai et al. (2023) characterized the pore structure and fluid distribution in deep marine shales for the Longmaxi Formation of southern Sichuan with low-temperature nitrogen adsorption, scanning electron microscopy, and nuclear magnetic resonance experiments.

Permeability is a pivotal parameter for evaluating the potential associated with oil and gas reservoir exploitation. Establishing a quantitative relationship between permeability and reservoir petrophysical properties at logging or seismic band is critical for an efficient shale oil production. This relationship was initially derived based on experimental data. For instance, Timur (1968) experimentally measured the permeability, porosity, and residual water saturation of 155 sandstone samples from various North American oil fields, establishing a rational relation for estimating sandstone permeability, and suggesting that an empirical relation can be the most effective approach regarding this purpose. Walls (1982) analyzed the impact of pore pressure, confining pressure and partial saturation on permeability through a series of experiments, concluding that permeability decreases with increasing effective pressure (confining pressure minus pore pressure) or water saturation. Yale (1984) quantified the permeability and electrical conductivity of tight sandstones under varying effective pressures and revealed that both properties substantially decline with increasing pressure. Prasad (2003) proposed a relationship between sonic logging velocity and permeability by categorizing rocks into the hydraulic power units, which was verified with the extensive laboratory data. Benson et al. (2006) investigated the effects of microstructure on elastic anisotropy and transport properties by conducting rock physical experiments on basalt and granite. They compared laboratory measurements with predictions from an effective permeability model, successfully elucidating the permeability and porosity variation patterns under pressure. Katayama et al. (2020) analyzed the relative variation of permeability profiles within the crust–mantle sequences of Samail ophiolite based on the experimentally-measured resistivity data from dry and saturated rocks and the effective medium theory. Lu et al. (2023) investigated the potential relationships between permeability, porosity, and aspect ratios of pores and cracks in artificial sandstones with similar porosities but different permeabilities, according to the rock experiments and a double porosity model. They found that compliant porosity is the primary influence of the sandstone permeability divergence.

By considering that the relationship between permeability and physical properties of rocks established with experimental data may be nonunique, it cannot be directly applied to logging or seismic scales. Subsequently, Coates and Dumanoir (1974) proposed the

relationship between porosity and formation resistivity at irreducible water saturation and provided a methodology for deriving permeability from logging data. Based on the multiple regression analysis, Khandelwal and Ranjith (2010) established a statistical model to connect petrophysical logging responses with formation permeability. Slagle and Goldberg (2011) presented a novel approach to compute porosity from resistivity logging data and estimated permeability at Site 1256 of the shallow oceanic crust through an empirical porosity–permeability relationship. Al-Dughaimi et al. (2021) measured porosity, permeability, and P- and S-wave velocities of 18 tight sandstone samples subjected to varying effective pressures and established the permeability–stress, porosity–stress, and velocity–stress relations based on the experimental data. They derived the relationship between acoustic impedance and permeability. However, the relation was not evaluated with the actual data from logging or seismic bands. Zhang et al. (2022) analyzed the variations of measured formation resistivity data with different permeabilities during various periods. They proposed a permeability modeling approach based on the time-shifted resistivity logging data without considering the variations in relative permeability curves across different reservoirs. Roberto et al. (2023) developed an iterative geostatistical seismic inversion method, by combining the precalibrated rock physical models and geostatistical modeling methods. They employed seismic data to predict reservoir permeability but did not extend this work to the prestack seismic inversion.

Neural network methods offer substantial assistances for estimating permeability from geophysical logging responses (Rezaee et al., 2008). Helle et al. (2001) used a back propagation neural network (BPNN) simulation to predict permeability by incorporating density, gamma rays, neutron porosity, and sonic wave velocity as input. Yasin et al. (2018) introduced a method combining neural network (NN), multiple variable regression, and classification of data mining to estimate permeability from conventional logging data, while it is failed for the highly-heterogeneous reservoirs. Khalifah et al. (2019) predicted permeability within tight carbonate reservoirs by using the artificial neural networks and genetic algorithms, where the input parameters included porosity, pore throat size, and formation factors. Zhao et al. (2022) estimated the permeability of low-permeability sandstone reservoirs with logging data, by applying 7 machine-learning methods, including linear regression, back propagation neural network regression, k-neighbors regression, random forest regression, support vector machine regression, gradient boosting decision tree regression, and extreme gradient boosting (XGBoost) decision tree regression. Their study successfully predicted the continuous permeability profile of a well. Mulashani et al. (2022) introduced a data managing approach based on the reformulated Levenberg–Marquardt (LM) method, where the input variables include natural gamma ray, effective porosity, shale volume, and thermal neutron porosity logging data. The accuracy of log permeability prediction is improved. Nevertheless, these methods depend on the reliability of data and require sufficient time for network training and testing.

By expanding the work of Al-Dughaimi et al. (2021), this study selects 21 tight sandstone samples from the shale oil formations of Ordos Basin Q area and measures the porosity, permeability, ultrasonic velocities, and resistivity under varying pressures. With the experimental data, relationships between P-wave impedance–permeability and resistivity–permeability at logging and seismic scales are established. Subsequently, these relationships are applied to well logging and seismic data for testing and the comparative analysis.

Geological background and general situation of the work area

The Ordos Basin is one of the most crucial oil-bearing basins of China, located at the intersection of the eastern and western tectonic regions, where the target formation is the Chang 7 member of the Yanchang Formations in the Q area, which is located at the southern segment of the basin. It can be further divided into Chang 7_1, 7_2, and 7_3 layers from top to bottom. The samples of this experiment are primarily collected from the Chang 7_1 and 7_2 layers. These reservoirs predominantly comprise fine-grained clastic rocks, with Chang 7_1 and 7_2 layers consisting mainly of silt-fine sandstones interbedded with mud/shale.

Experimental samples and processes

1. Experimental samples

The porosities (permeabilities) of experimental

samples range from 3.56% (0.005 mD) to 10.16% (0.096 mD). X-ray diffraction analysis indicates that mineralogical composition (Table 1) mainly comprises quartz, feldspar, plagioclase and clay. Furthermore, thin sections of samples 1 and 2 show that there are pores and cracks in these samples (Figure 1).

Table 1 Physical properties and mineral composition of rock samples

Number	Core number	Density (g/cm^3)	Porosity (%)	Permeability (mD)	Quartz (%)	Feldspar (%)	Plagioclase (%)	Calcite (%)	Ankerite (%)	Dolomite (%)	Siderite (%)	Pyrite (%)	Clay (%)
1	1-2	2.41	9.252	0.072	57.80	5.45	19.75	2.91	-	5.88	1.99	-	6.22
2	1-3	2.44	9.201	0.038	56.15	5.20	19.33	3.85	-	5.68	2.67	-	7.12
3	1-5	2.48	7.259	0.015	57.11	4.71	20.88	1.96	-	6.92	1.82	-	6.60
4	1-8	2.49	6.376	0.018	52.42	5.66	21.60	6.78	-	5.69	1.62	-	6.23
5	1-10	2.54	5.625	0.006	48.97	7.70	15.43	0.31	11.46	10.12	0.91	-	5.10
6	1-12	2.49	7.220	0.020	48.59	7.90	18.66	2.02	6.96	8.95	1.05	-	5.87
7	1-17	2.44	5.208	0.012	50.93	9.05	22.42	3.08	2.88	4.77	0.75	-	6.12
8	1-19	2.44	5.065	0.018	52.35	6.20	25.35	4.17	2.37	3.43	0.54	-	5.59
9	1-20	2.57	4.491	0.033	47.73	6.40	17.91	1.96	2.72	6.65	1.05	0.35	15.23
10	1-23	2.41	8.998	0.078	56.81	8.39	21.24	1.10	-	7.05	0.80	-	4.61
11	1-24	2.47	7.674	0.074	49.46	8.20	26.36	2.91	-	6.99	0.89	-	5.19
12	1-28	2.46	7.547	0.043	60.78	6.96	21.72	2.15	0.93	1.15	1.80	0.17	4.34
13	1-29	2.51	5.787	0.020	52.47	7.60	22.47	2.34	2.77	3.32	1.19	-	7.84
14	1-30	2.53	5.278	0.005	50.95	6.71	19.96	1.96	2.23	4.82	2.41	-	10.96
15	2-1	2.48	7.327	0.019	55.40	6.26	19.81	2.06	2.60	6.30	1.72	-	5.85
16	2-2	2.57	4.819	0.017	53.87	6.84	18.08	2.91	3.15	6.82	1.17	-	7.16
17	2-3	2.41	8.847	0.065	56.77	7.23	21.26	1.96	1.34	2.91	2.98	-	5.55
18	2-4	2.41	6.156	0.016	42.46	6.92	13.65	0.99	20.46	9.99	0.52	0.39	4.62
19	2-5	2.44	7.787	0.042	51.06	8.78	21.27	6.60	2.03	3.33	1.64	-	5.29
20	2-6	2.48	5.235	0.015	40.44	9.37	19.84	20.81	2.46	2.91	0.71	-	3.46
21	2-10	2.49	8.791	0.056	55.69	4.61	20.79	4.16	2.33	5.47	0.86	-	6.09

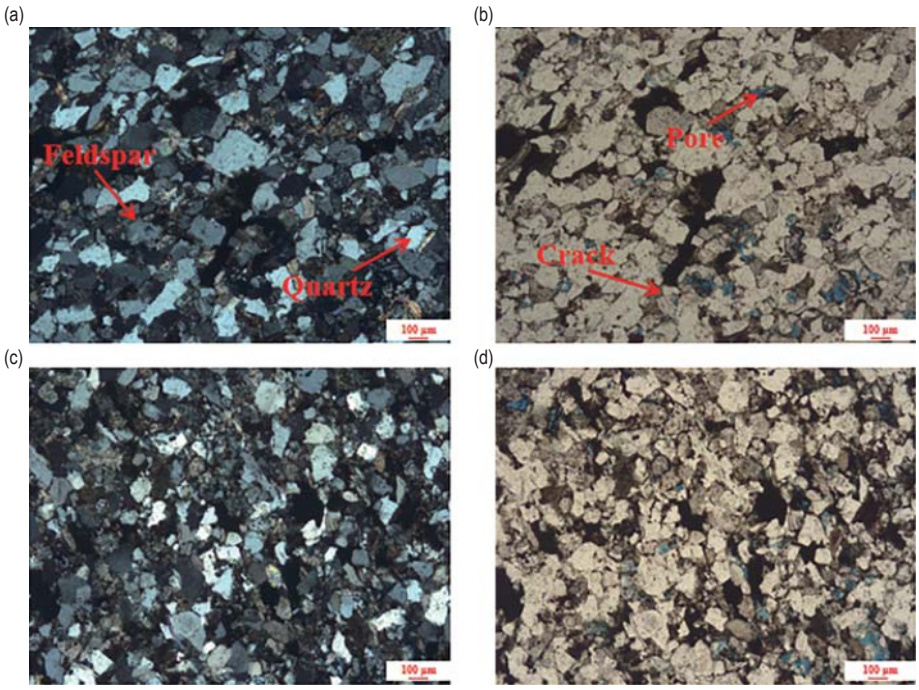

Figure 1. Thin sections of tight sandstone samples 1 (a, b) and 2 (c, d) in the target formation; the blue area indicates the pore space.

2. Experimental processes

(1) Porosity and permeability measurements

Porosity and permeability measurements are conducted by using a helium porosimeter permeameter based on the pulse attenuation method (Yang and Dong., 2017), where porosity is determined by using the helium expansion method, and permeability by using the unsteady-state pulse transient decay technique corrected by the Klinkenberg slippage effect (Klinkenberg, 1941). During the experiment, the confining pressures are sequentially set at 5, 15, 25, 35, and 45 MPa, and the pore pressure is maintained a constant value of 0 MPa. The temperature is held at room temperature (~20°C).

(2) Ultrasonic velocity measurements

Ultrasonic velocity experiments are performed at room temperature (~20°C) by using nitrogen as the pore fluid. The confining and pore pressures are initially increased to 5 MPa, and the latter remains constant. To prevent uneven distribution of pore pressure within the sample induced by excessively rapid confining pressure loading, the former is loaded with a stress rate of 0.1 MPa/min to P_c = 60 MPa, where they are set at 5, 10, 20, 30, 40, 50, and 60 MPa, and then unloaded to P_c = 5 MPa at the same rate. To allow for pore pressure equilibrium, the system stands still for a duration ranging from 30 minutes to 2 hours after each loading is completed. The P- and S-wave velocities of the samples are measured using ultrasonic sensors.

(3) Resistivity measurements

Resistivity measurements are implemented by using the two-electrode method. The procedure involves calibrating the resistivity probe. Subsequently, the samples, saturated by the water containing 5% NaCl, are installed with a pressurized unit. The confining pressures are 3, 5, 15, 25, 35, and 45 MPa, and the pore pressure remains at 0 MPa. The temperature is held at room temperature (~20°C). After achieving pressure stabilization, the electrical instrument is engaged for measurements. Voltage adjustments are made for repeated measurements, and the resistivity of the sample is subsequently calculated.

3. Experimental results

(1) Porosity and permeability

Figures 2a and 2b illustrate the porosity (ϕ) and permeability (κ) of 21 samples under different effective pressures. As is expected, the porosity and permeability demonstrate nonlinear decreases within the low effective pressure range as the effective pressure increases. Conversely, they exhibit nearly linear decreases within

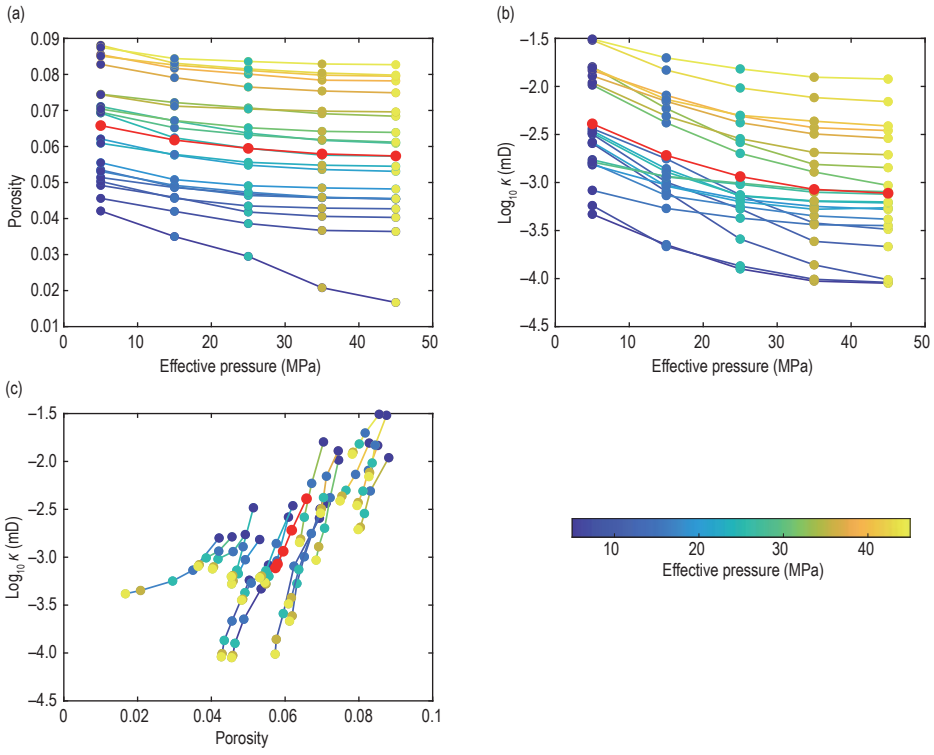

Figure 2. Porosity (a) and the decimal logarithm of permeability (b) as a function of effective pressure, and the decimal logarithm of permeability as a function of porosity (c); the red circle denotes the arithmetic averages of the measurements.

the high effective pressure range. This behavior can be attributed to the gradual closure of cracks with low aspect ratios in the rocks with increasing pressure (Walsh, 1965; Watanabe et al., 2019; Zhang et al., 2022). Figure 2c shows the relationship between permeability and porosity, demonstrating that permeability increases with increasing porosity. Moreover, the decimal logarithm of permeability presents a better linear correlation with porosity.

Following the work of Al-Dughaimi et al. (2021), the relationships between the arithmetic averages of porosity and permeability (decimal logarithm) and effective pressure are established as

$$\log_{10}\kappa = -1.123\sqrt{\frac{P}{45}} - 2.051, \tag{1}$$

$$\phi = 10^{-0.09275\sqrt{\frac{P}{45}}-1.153}, \tag{2}$$

where the dimension of permeability (effective pressure) is mD (MPa). The relationships are compared with those observed in tight gas sandstones, as provided by Al-Dughaimi et al. (2021):

$$\log_{10}\kappa = -2.3718\sqrt{\frac{P}{50}} + 0.0495, \tag{3}$$

$$\phi = 0.035 + 10^{-0.79\sqrt{\frac{P}{50}}-1.64}. \tag{4}$$

The comparative results are illustrated in Figure 3, indicating that these relationships are highly similar in the two cases. Moreover, the relative errors between the arithmetic averages of the measured data and the fitted results are all less than 1%. The red circles in the figure signify the average values of porosity and permeability of the measured samples. The average porosity (permeability) decreases from 6.58% (3.2 mD) to 5.74% (2.4 mD). Although the microcracks are well-developed within the rocks, they exhibit poor connectivity. Additionally, the rocks contain a certain amount of clay minerals, and are relatively tight. These factors contribute to the insensitivity of both parameters to pressure variations. Moreover, Al-Dughaimi et al. (2021) also employed the Kozeny–Carman equation (Mavko et al., 2009) to establish an empirical relationship between the decimal logarithm of permeability and porosity:

$$\log_{10}\kappa \approx 4.95 + 3\log_{10}(\phi - 0.035). \tag{5}$$

Similarly, a relationship is deduced from the measurements in this study as

$$\log_{10}\kappa \approx 2.7 + 3\log_{10}(\phi - 0.046), \tag{6}$$

where the percolation porosity in Equation (6) is 0.046, slightly larger than 0.035 of Equation (5) provided by Al-Dughaimi et al. (2021). Typically, the percolation porosity ranges from 0.02 to 0.05 (Mavko et al., 1997).

(2) Ultrasonic velocities

Figure 4 shows P- and S-wave velocities (V_p and V_s) and Poisson's ratio (v) as a function of the effective pressure during unloading. Results reveal a rapid increase in velocity at low effective pressures, while at high effective pressures, velocity exhibits a linear increase, which is also related to the presence of cracks in the rocks. The average P-wave velocity increases from 4.28 km/s to 4.89 km/s, whereas the average S-wave velocity increases from 2.77 km/s to 3.08 km/s. In contrast, Poisson's ratio exhibits a gradual increase as the pressure increases, with minimal fluctuations observed across the entire pressure range. It is

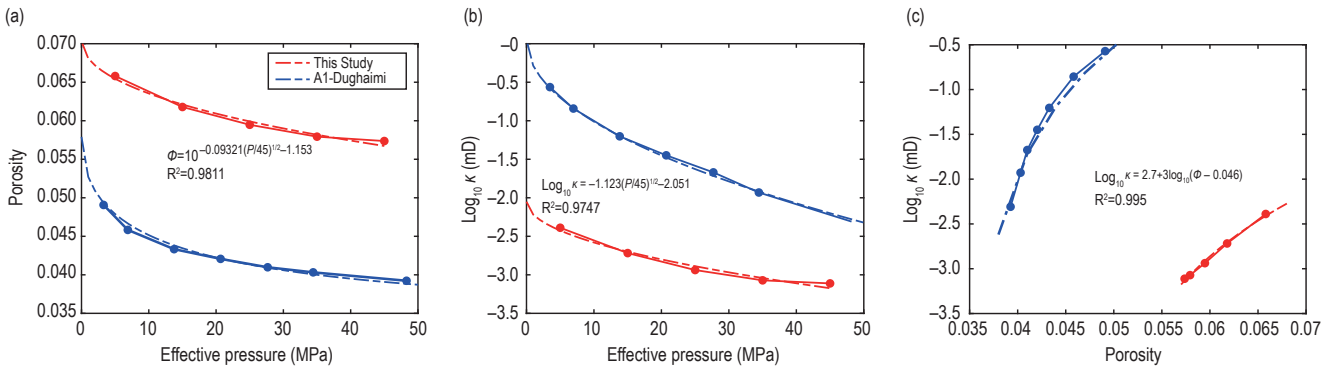

Figure 3. Arithmetic averages of porosity (a) and decimal logarithm of permeability (b) as a function of the effective pressure; arithmetic average of porosity as a function of decimal logarithm of permeability (c); the blue circles denote measurements of Al-Dughaimi et al. (2021); the red circles correspond to the measurements of this study; the dashed line represents the fitting relationship.

noteworthy that, except for sample 2-6, Poisson's ratios of the experimental samples mainly fall within the range of 0.12 to 0.20. This range is similar to Poisson's ratio distribution (0.05–0.20) reported for tight sandstones in the study by Al-Dughaimi et al. (2021). The difference can be attributed to the higher calcite content with 0.29–0.32 of Poisson's ratio, in sample 2-6 compared to the other samples (Table 1). Consequently, it results in the Poisson's ratio distribution range of 0.23–0.25 for sample 2-6, which is greater than the values observed in the other samples.

To establish the relationship between elastic wave velocities and porosity/permeability of tight sandstone samples, the measured porosity and permeability are resampled based on the effective pressures employed in the ultrasonic experiments. Figures 5a and 5b illustrate the P- and S-wave velocities as a function of porosity. Results show that the velocities decrease with increasing porosity. Throughout the unloading process, the average porosity increases from 0.056 to 0.07, and the average P- (S-) wave velocity decreases from 4.89 (3.08) km/s to 4.28 (2.77) km/s. Figures 5c and 5d show the variations in P-wave and S-wave velocities versus the logarithm of permeability. Velocities decrease with increasing permeability, accompanied by a corresponding increase in the average permeability from 2.067 mD to 3.292 mD. Figures 5e and 5f display porosity/permeability with respect to P-wave impedance. Permeability and porosity decrease with increasing impedance. The comparison with the arithmetic averages of corresponding parameters

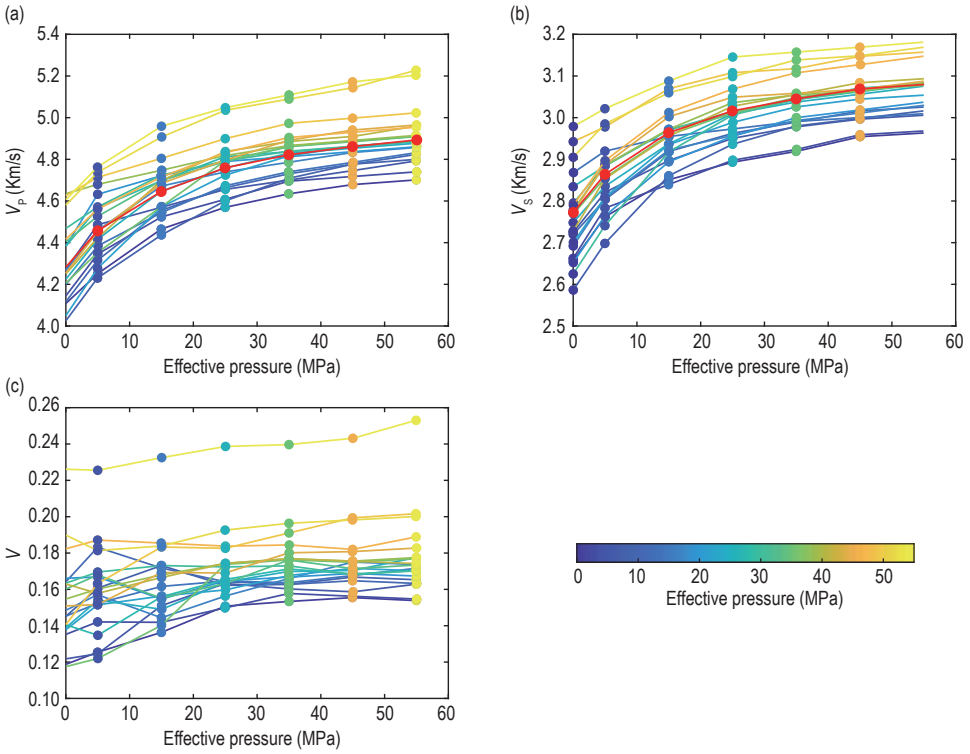

Figure 4. P- (a) and S-wave velocities (b), and Poisson's ratio (c) as a function of effective stress; the red circles represent the arithmetic averages of the measurements.

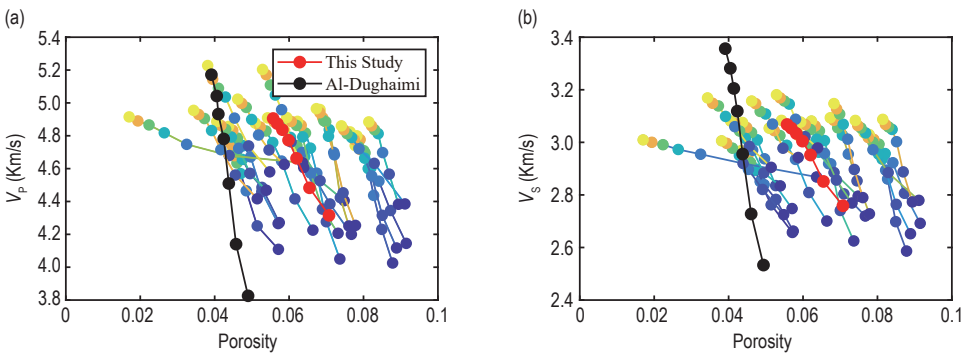

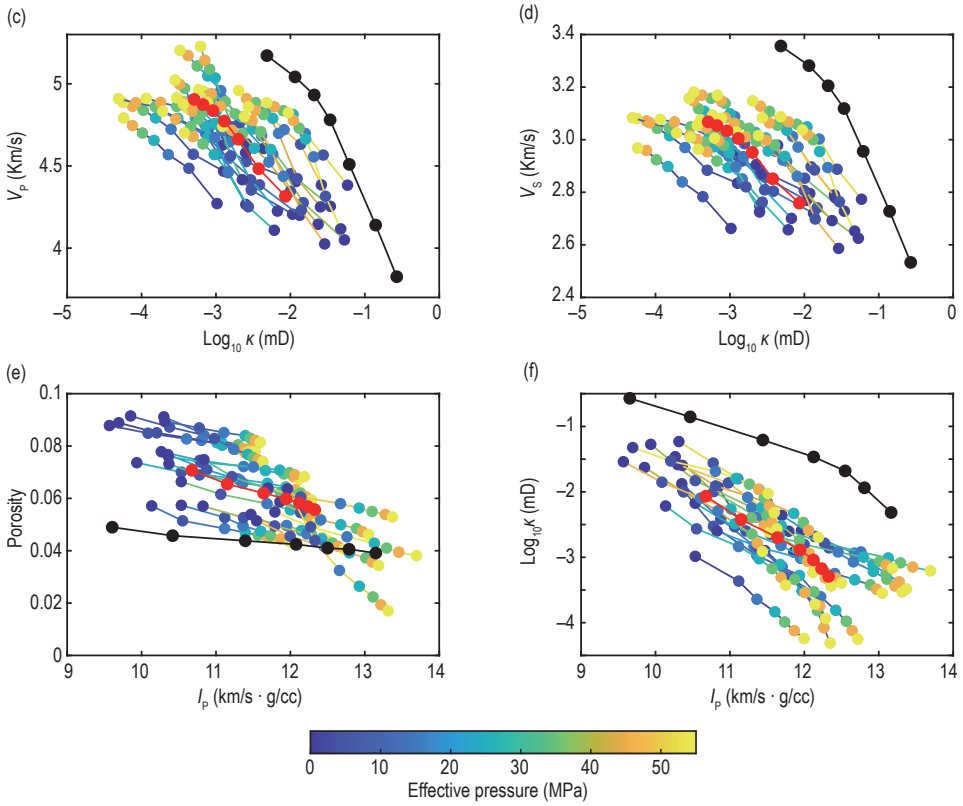

Figure 5. P- (a) and S-wave (b) velocities as a function of porosity, P- (c) and S-wave (d) velocities as a function of decimal logarithm of permeability, and porosity (e) and decimal logarithm of permeability (f) as a function of P-wave impedance. The black circles represent the arithmetic averages of the measurements of Al-Dughaimi et al. (2021), and the red circles correspond to the measurements of this study.

presented by Al-Dughaimi et al. (2021) (black curves) shows that the variation trend of the experimental data in this study is consistent with that of their samples. The red curves of Figures 5a–5d indicate that in contrast to porosity, permeability exhibits a more substantial response to the changes in P-wave velocity, and the slope of the impedance–permeability relationship (Figure 5f) is larger than that of the impedance–porosity relationship (Figure 5e).

(3) Resistivity

Figure 6a shows resistivity as a function of effective pressure. Furthermore, resistivity exhibits nonlinear variations with increasing effective pressure, which is related to the presence of cracks within the rocks. The average resistivity increases from 25.89 Ω·m to 60.11 Ω·m. Figures 6b and 6c depict the relationship between porosity/permeability and resistivity. Porosity and permeability decrease as resistivity increases.

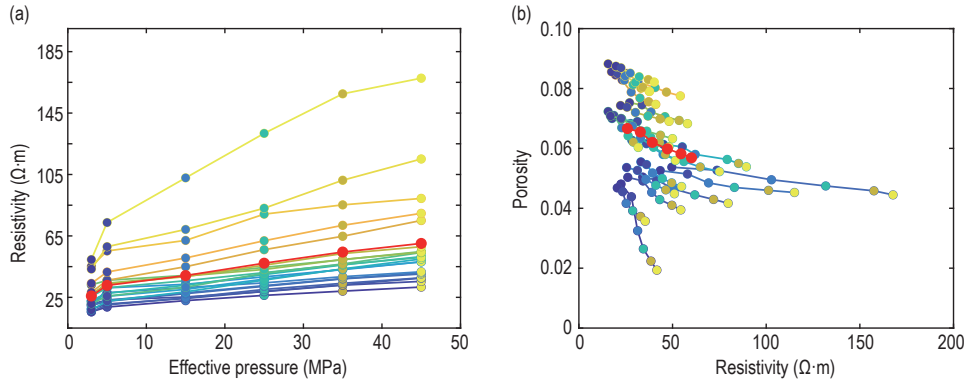

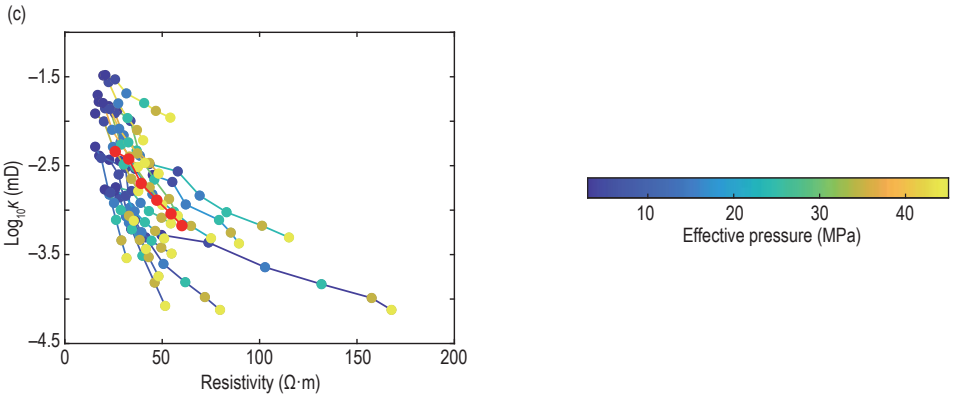

Figure 6. Resistivity (a) as a function of effective pressure, and porosity (b) and decimal logarithm of permeability (c) as a function of resistivity. The red circles represent the arithmetic averages of the measurements.

Comparing Figure 6c and Figure 6b shows that the effect on resistivity by permeability is more pronounced in contrast to that by porosity, where a sharp decrease in permeability typically accompanies an increase in resistivity.

Impedance–permeability and resistivity–permeability relations on logging and seismic scales

Following the work of Al-Dughaimi et al. (2021), this study establishes impedance–permeability and resistivity–permeability relationships on logging and seismic scales based on the aforementioned experimental data. The effective elastic moduli of the samples under different effective pressures are determined by using the Hashin–Shtrikman (HS) equation (Hashin and Shtrikman, 1963). It is assumed that the composite material is composed of 21 elements with the identical volume fraction, where the bulk and shear moduli of each element correspond to the elastic moduli of each of the 21 samples at stress state. The equations for these bounds are

$$K_{\mathrm{HS}\pm} = \left[\sum_{i=1}^{N} \frac{f_i}{K_i + \frac{4}{3}G_{\pm}}\right]^{-1} - \frac{4}{3}G_{\pm}, \tag{7a}$$

$$G_{\mathrm{HS}\pm} = \left[\sum_{i=1}^{N} \frac{f_i}{K_i + Z_{\pm}}\right]^{-1} - Z_{\pm}, \tag{7b}$$

$$Z_{\pm} = \frac{G_{\pm}}{6}\frac{9K_{\pm} + 8G_{\pm}}{K_{\pm} + 2G_{\pm}}, \tag{7c}$$

where $K_{\mathrm{HS}\pm}$ ($G_{\mathrm{HS}\pm}$) represents the upper and lower bounds of the bulk (shear) modulus, and K_+ (G_+) and K_- (G_-) denote the maximum and minimum bulk (shear) moduli, respectively. f_i is the volume fraction of the i-th elastic element, which is 1/21, and N = 21 is the number of samples. Figure 7 depicts the calculated P- and S-wave

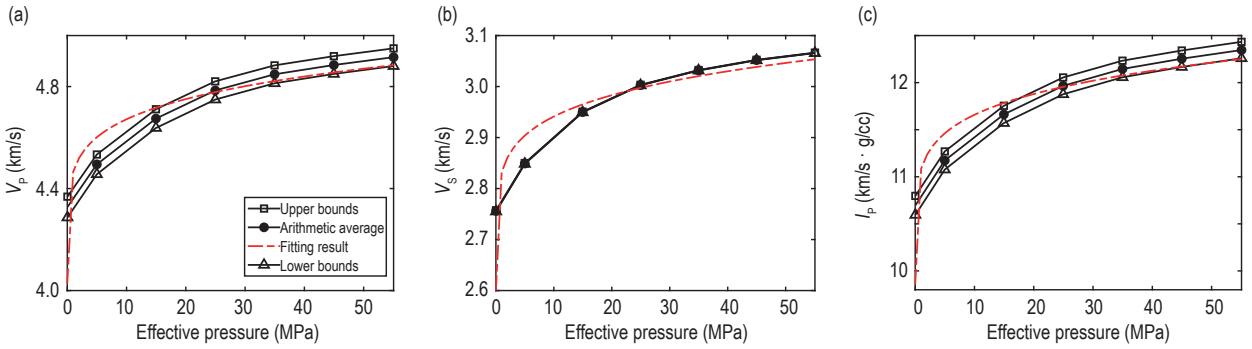

Figure 7. Upper and lower Hashin–Shtrikman (HS) bounds of P- (a) and S-wave (b) velocities and P-wave impedance (c) as a function of effective pressure. The black circles represent the arithmetic averages, and the red dashed lines represent the corresponding fitting curves with Equations (8)–(10).

velocities, the P-wave impedance, and their upper and lower bounds with the HS equations. Results reveal small variation between these upper and lower HS bounds. Then, the arithmetic average of these bounds can be employed to represent the effective velocity and impedance at each pressure point. Based on the fitting equation form established by Al-Dughaimi (2021) for the 18 tight gas sandstone samples and the calculated results of Equation (7), the fitting relations between V_{PEff}, V_{SEff}, I_{PEff} and effective pressure are

$$V_{\mathrm{PEff}} = 4.027+0.4393P^{\frac{1}{6}}, \tag{8}$$

$$V_{\mathrm{SEff}} = 2.6+0.2325P^{\frac{1}{6}}, \tag{9}$$

$$I_{\mathrm{PEff}} = 9.859+1.226P^{\frac{1}{6}}, \tag{10}$$

where the dimension of velocity (V_{PEff} and V_{SEff}) is km/s, and the dimension of P-wave impedance (I_{PEff}) is km/s·cm^3. The fitting results are given as the red curves in Figure 7, and the fitting coefficients R^2 are 0.9355 (V_{PEff}), 0.9451 (V_{SEff}), and 0.937 (I_{PEff}).

Furthermore, the HS equation is employed to simulate the upper and lower bounds of resistivity under each effective pressure:

$$R_{\mathrm{HS}\pm} = \left\langle \frac{f_i}{R_i + 2R_{\pm}} \right\rangle^{-1} - 2R_{\pm}, \tag{11}$$

where $R_{\mathrm{HS}\pm}$ represents the upper and lower bounds of resistivity, R_+ and R_- denote the maximum and minimum resistivity, respectively. R_i is the resistivity at the i-th effective pressure. The simulated results are displayed in Figure 8a. The arithmetic average of upper and lower bounds is used to represent the effective resistivity at each pressure, and the fitting relation between resistivity and effective pressure is as follows (red dashed curves in Figure 8a).

$$R_{\mathrm{Eff}} = -24.89+41.47P^{\frac{1}{6}}, \tag{12}$$

where the dimension of resistivity R_{Eff} is Ω·m.

Finally, according to Dvorkin (2009), the upper and lower bounds of sample permeability are calculated by using the arithmetic (κ) and harmonic $\left(\kappa^{-1}\right)^{-1}$ averages, and the simulated results are presented in Figure 8b. The arithmetic averages of upper and lower bounds are considered as the effective permeabilities, and the fitting relation between the permeability and effective pressure is (red dashed curves in Figure 8b)

$$\log_{10}\kappa = -1.088\sqrt{\frac{P}{45}} - 2.37\,. \tag{13}$$

Substituting Equations (10) and (12) into Equation (13), we can derive an approximate empirical relation between the effective permeability and P-wave impedance/resistivity.

$$\log_{10}\kappa = -0.088(I_{\mathrm{P}} - 9.859)^3 - 2.37\,, \tag{14}$$

$$\log_{10}\kappa = -0.00000227(R + 24.89)^3 - 2.37\,. \tag{15}$$

Permeability prediction of tight sandstone based on multiscale data

1. Permeability prediction of tight sandstone at logging scale

We perform permeability predictions from the logging data based on the established relations of $I_{\mathrm{P}} - \kappa$ and

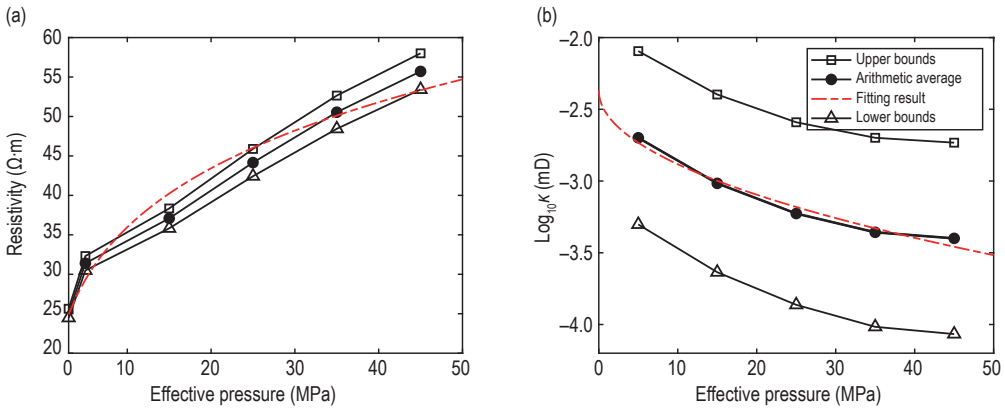

Figure 8. Upper and lower bounds of resistivity (a) and permeability (b) as a function of effective pressure; the red dashed curves are the fitting results of Equations (12) or (13).

$R - \kappa$ at the logging scale. Given that the experimental samples are predominantly sourced from the five wells in the Ordos Basin Q area, the predicted permeabilities from the relations of these five wells are individually presented in Figures 9–13, and compared with the permeability values interpreted of the original logging data. This section adopts the maximum value of each data set as a reference, normalizes the data, and takes the logarithm simultaneously to compare the variation trends of the measured and predicted values. The compared results of each well are displayed in Figures 9f–13f. The blue curve represents the permeability interpreted of the logging data, the red curve represents the predicted permeability by using the established $I_P - \kappa$ relationship, and the brown curve corresponds to the predicted result with the established $R - \kappa$ relationship. The comparison reveals that the predicted permeability curves from the $I_P - \kappa$ relationship have a similar trend to the interpreted data, demonstrating a good overall correlation. This result indicates that the established empirical

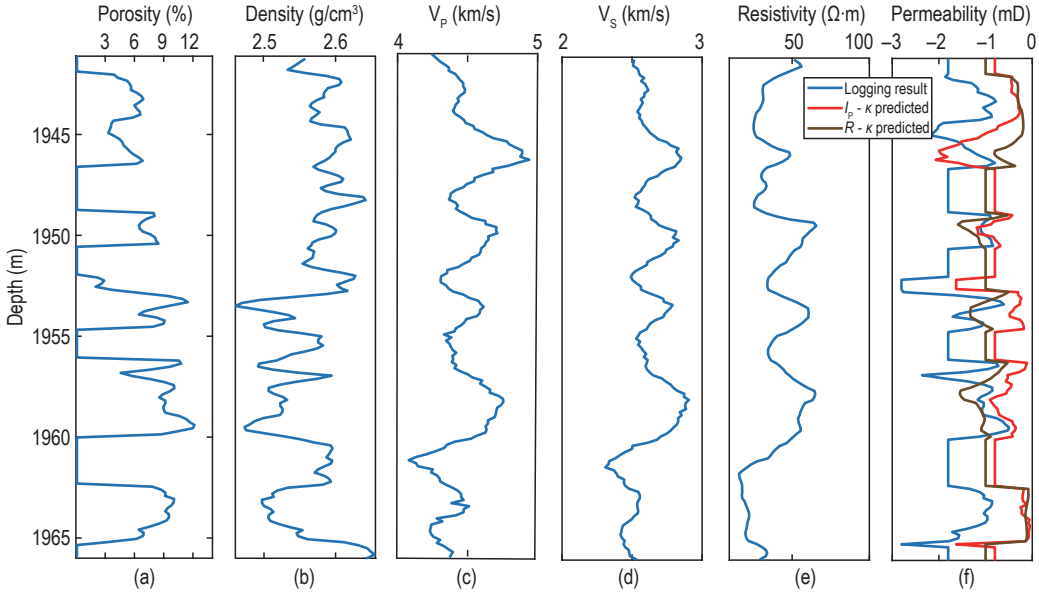

Figure 9. Comparison of predicted and interpreted permeabilities of well 1: (a) porosity; (b) density; (c) P-wave velocity; (d) S-wave velocity; (e) resistivity; (f) permeability.

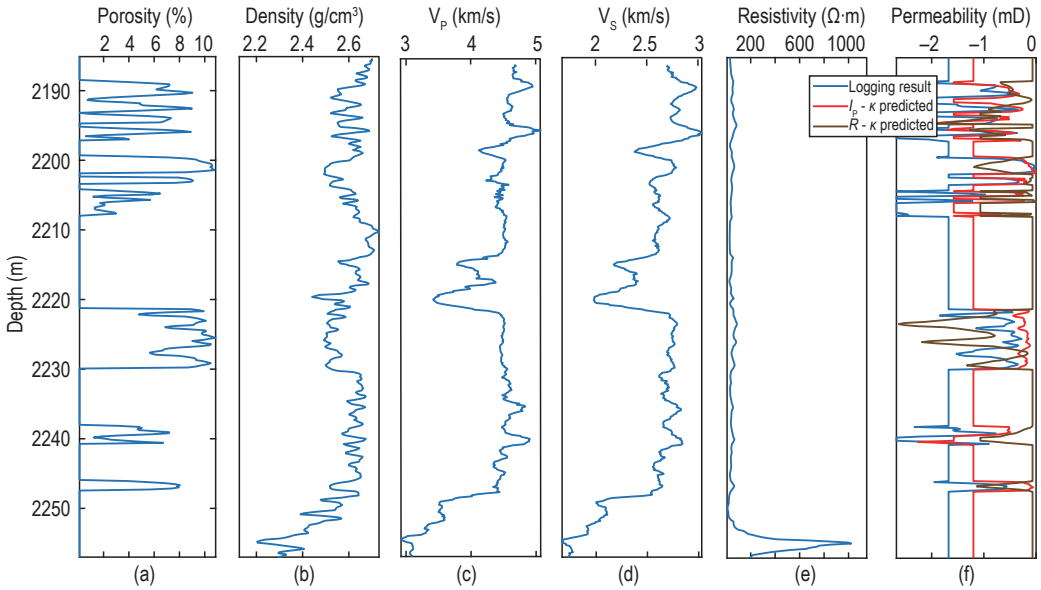

Figure 10. Comparison of predicted and interpreted permeabilities of well 2. (a) porosity; (b) density; (c) P-wave velocity; (d) S-wave velocity; (e) resistivity; (f) permeability.

relationship can reasonably describe the permeability variation characteristics of Chang 7_1–7_2 layers. A further comparison between the predicted results of the five wells indicates that the accuracy of permeability prediction is higher for sandstone intervals with higher porosity. Among them, well 3 exhibits a generally high porosity, with the entire interval mostly exceeding 8%. Therefore, it exhibits the best overall fittings, validating the validity of $I_P - \kappa$. Regarding the $R - \kappa$ relationship, the predicted results also exhibit a similar trend to the interpreted data, while there are opposing trends in some depth ranges of well 1 (1957–1959 m), well 2 (2221–2230 m), well 3 (2127–2138 m) and well 5 (1923–1926 m, 1949–1955 m). This feature indicates that the prediction from the $R - \kappa$ relationship is worse than that with the former relationship.

Figure 14 reports the error analysis results of the predicted and interpreted permeabilities. The blue line represents the error bar between the two data sets. The error between the two data sets is small, and the overall

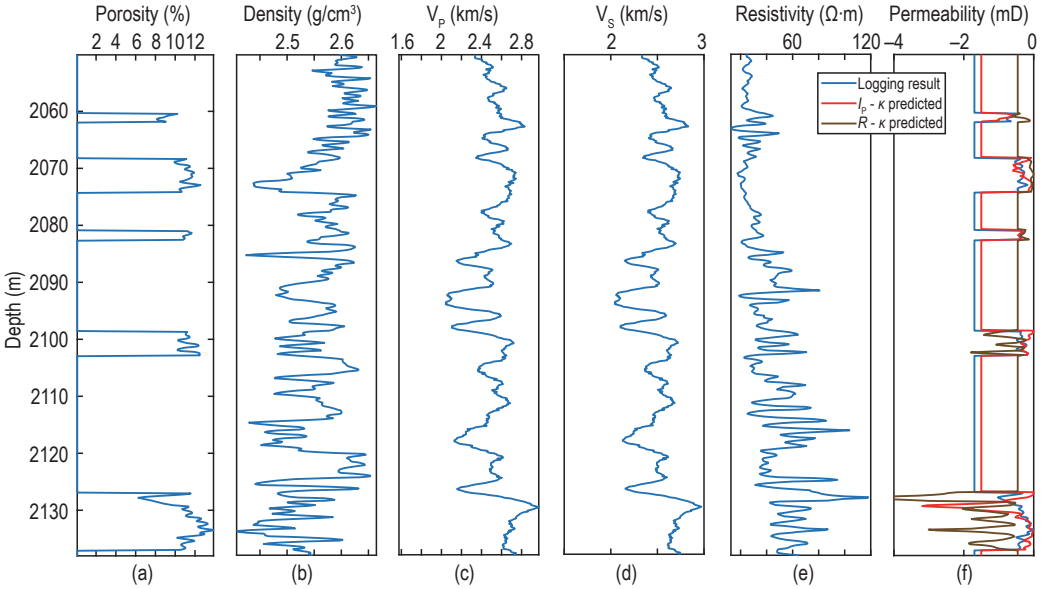

Figure 11. Comparison of predicted and interpreted permeabilities of well 3. (a) porosity; (b) density; (c) P-wave velocity; (d) S-wave velocity; (e) resistivity; (f) permeability.

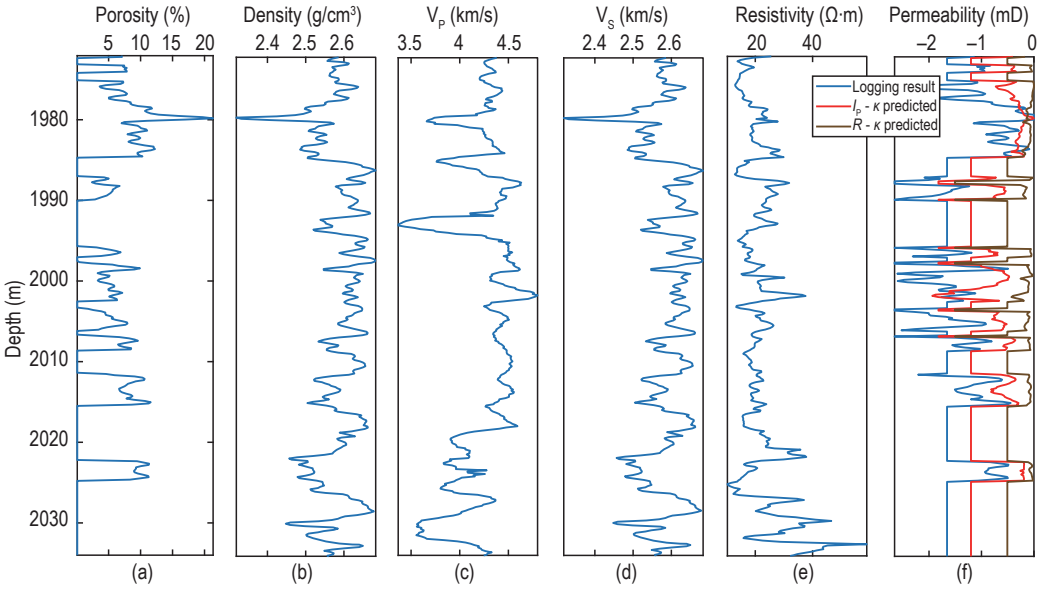

Figure 12. Comparison of predicted and interpreted permeabilities of well 4. (a) porosity; (b) density; (c) P-wave velocity; (d) S-wave velocity; (e) resistivity; (f) permeability.

error is distributed around 0. Combined with the overall variation trends in Figures 9–13, this result indicates that the established $I_P - \kappa$ relationship can be used to effectively predict permeability at the logging scale. The established relationships in this study can be applied to tight sandstones at various depths.

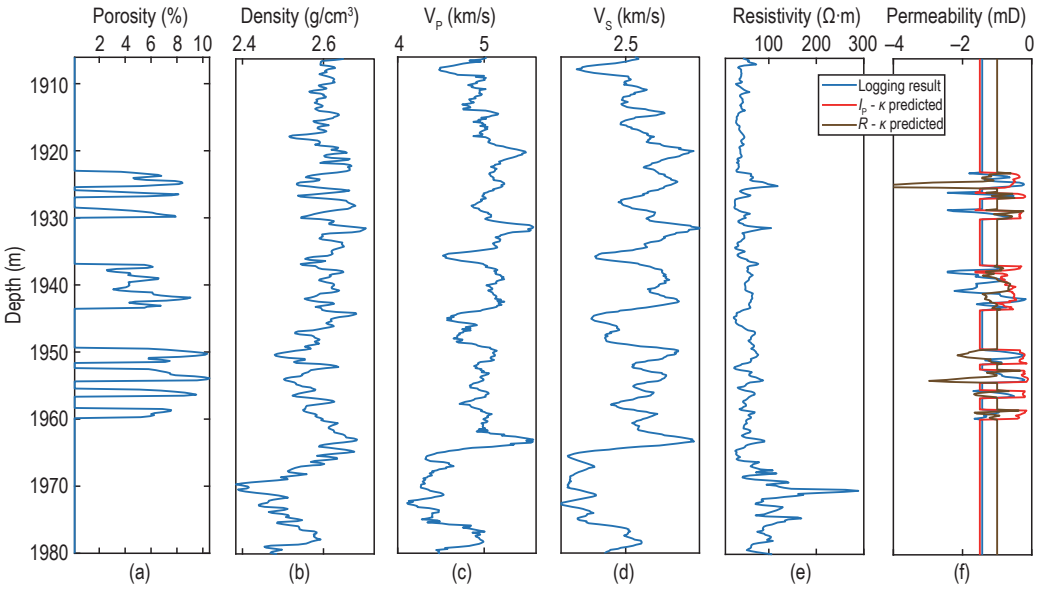

Figure 13. Comparison of predicted and interpreted permeabilities of well 5.
(a) porosity; (b) density; (c) P-wave velocity; (d) S-wave velocity; (e) resistivity; (f) permeability.

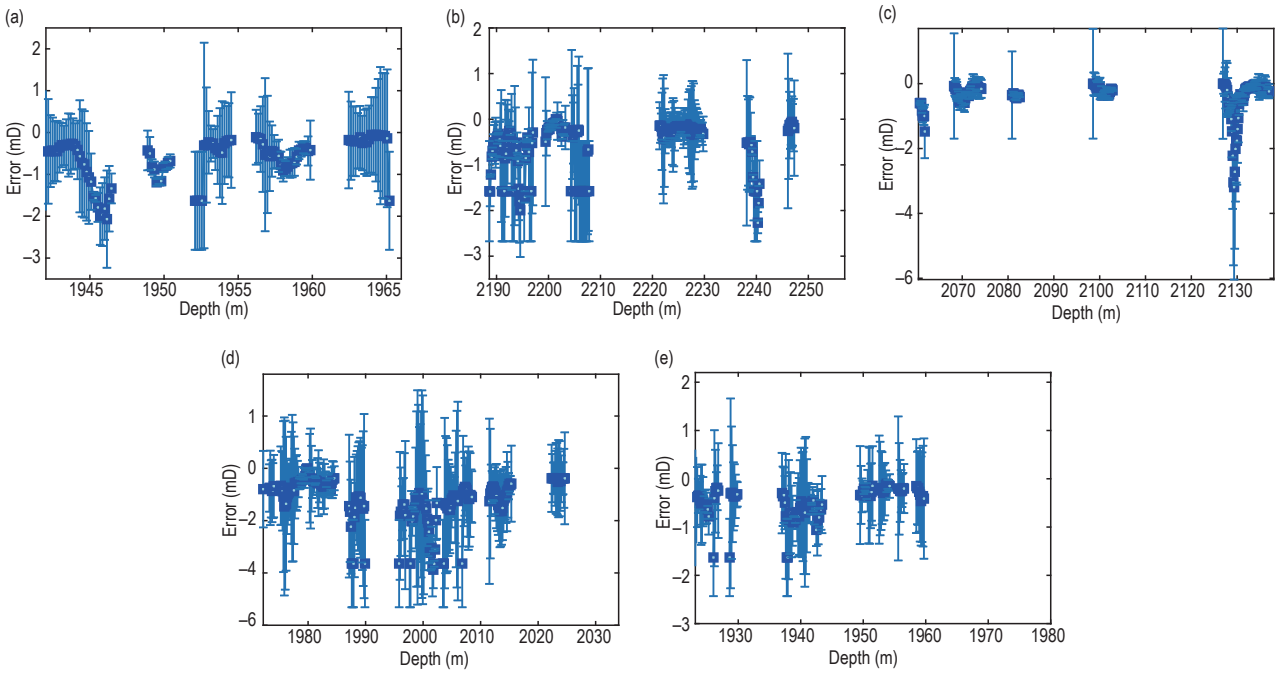

Figure 14. Error analysis results of predicted and interpreted permeabilities.
(a) well 1; (b) well 2; (c) well 3; (d) well 4; (e) well 5.

2. Permeability prediction based on seismic data

Permeability prediction at the seismic scale is performed by using the established $I_P - \kappa$ relationship. In this section, we predict permeability of a 2D seismic profile crossing wells 4, 6, and 7. By utilizing the P-wave impedance inverted from the original 2D seismic

data, permeability is calculated with the established relationship.

Figure 15a illustrates I_P obtained from the seismic data. From top to bottom, the target layer is divided into the Chang 7_1 and 7_2 Layers. I_P of the three wells across the entire reservoir sections primarily lies within 9–13 km/s·cm^3. Wells 4 and 6 exhibit lower impedance, whereas well 7 has a higher impedance. Additionally, the overall P-wave impedance of Chang 7_1 layer is relatively high.

The predicted permeability profile is given in Figure 15b. The permeability within the target layer predominantly ranges from 0.0001 mD to 0.008 mD. Chang 7_1 of wells 4 and 6 shows higher permeability, around 0.007 mD, whereas well 7 exhibits a lower value. Chang 7_2 of well 4 has the highest permeability. It is apparent that well 7, having a higher P-wave impedance, corresponds to lower permeability in the target layer. In contrast, well 4 with a low P-wave impedance is associated with higher permeability. Figure 16 presents the seismic prediction profile around well 4. Results show that well 4 has a good oil reserve capacity. According to the actual conditions of the working area, it is evident that the Chang 7_1 and 7_2 layers primarily comprise sandstone, with Chang 7_2 containing the primary oil reservoirs due to its high porosity and abundant reservoir spaces. The actual production data indicates that well 4 has yielded a cumulative oil production of 528.7 t, whereas wells 6 and 7 in the target zone show no industrial production yet. The predicted results agree with the actual situation.

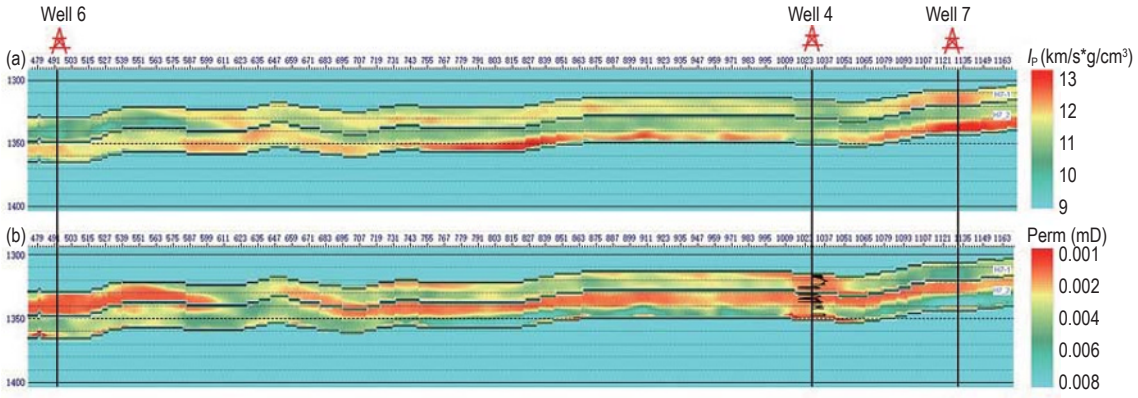

Figure 15. 2D seismic profiles crossing wells 4, 6, and 7: (a) P-wave impedance; (b) permeability prediction profile.

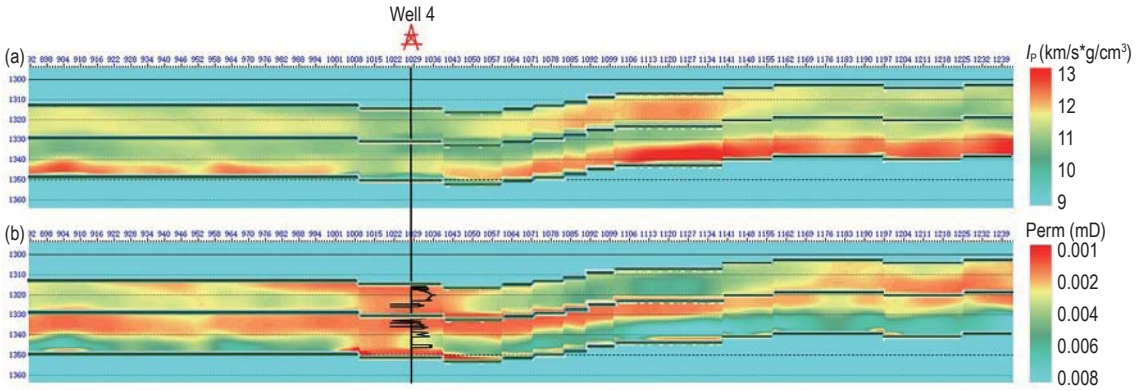

Figure 16. 2D seismic profile around well 4: (a) P-wave impedance; (b) permeability prediction profile.

Conclusions

Based on the experimental data of the 21 tight sandstones collected from the Ordos Basin, we analyze the variation of permeability versus porosity, acoustic impedance and resistivity, and establish the $I_P - \kappa$ and $R - \kappa$ relationships at the ultrasonic scale. These relations are extended by combining the effective medium model and measurements for the logging and seismic scales. Comparing with the interpreted permeability of the original logging data demonstrates the effective

performance of the $I_P - \kappa$ relationship in contrast to the $R - \kappa$ relationship. Comparative analysis based on the seismic data further validates the effectiveness of the former relationship. Increasing the number of experimental samples and incorporating the impacts of frequency on the wave impedance can help improve the applicability and accuracy of this relationship. Alternatively, using NN methods for a further data training can be explored. The impedance–permeability relationship established in this study can be applied to predict the permeability of the target layers, providing a technical approach for assessing shale oil reservoir sweet spots.

Acknowledgments

The authors acknowledge the supports from the National Natural Science Foundation of China (42104110, 41974123, 42174161, and 12334019), the Natural Science Foundation of Jiangsu Province (BK20210379, BK20200021), the Postdoctoral Science Foundation of China (2022M720989), and the Fundamental Research Funds for the Central Universities (B210201032).

Reference

Al-Dughaimi, S., Muqtadir, A., Alzaki, T., et al., 2021, Stress dependence of elastic and transport properties in tight gas sandstones: Journal of Petroleum Science and Engineering, **196**, 108001.

Benson, P., Schubnel, A., Vinciguerra, S., et al., 2006, Modeling the permeability evolution of microcracked rocks from elastic wave velocity inversion at elevated isostatic pressure: Journal of Geophysical Research, **111** (b4).

Cai, G., Gu, Y., Jiang, Y., et al., 2023, Pore Structure and Fluid Evaluation of Deep Organic-Rich Marine Shale: A Case Study from Wufeng–Longmaxi Formation of Southern Sichuan Basin: Applied Sciences, **13**, 7827.

Coates, G. R., and Dumanoir, J. L., 1974, A New Approach To Improved Log-Derived Permeability: Log Analyst, **15**(1), 17–31.

Deng, J. X., Wang, H., Zhou, H., et al., 2015, Microtexture, seismic rock physical properties and modeling of Longmaxi Formation shale: Chinese Journal of Geophysics, **58**(06), 2123–2136.

Guo, Z. Q., Li, X. Y., Liu, C., et al, 2013, A shale rock physics model for analysis of brittleness index, mineralogy and porosity in the Barnett Shale: Journal of Geophysics and Engineering, **10**(1): 1–10.

Hosseiny, E., and Mohseni, A., 2023, Garau Formation as an unconventional hydrocarbon resource in southwestern Iran: a geochemical investigation: Journal of Petroleum Exploration and Production Technology, **13**, 1535–1549.

Helle, H, B., Bhatt, A., and Ursin, B., 2001, Porosity and permeability prediction from wireline logs using artificial neural networks: a north sea case study: Geophysical Prospecting, **49**(4), 431–444.

Jia, C. Z., Zheng, M., Zhang, Y. F., 2013, Unconventional hydrocarbon resources in China and the prospect of exploration and development: Petroleum Exploration and Development, **39**(02), 129–136.

Klinkenberg, L. J., 1941, The permeability of porous media to liquids and gases: Drilling and Production Practice, 200–213.

Khalifah, H. A., Glover, P. W. J., and Lorinczi, P., 2019, Permeability Prediction and Diagenesis in Tight Carbonates Using Machine Learning Techniques: Marine and Petroleum Geology, **112**, 104096.

Katayama, I., Abe, N., Hatakeyama, K., et al., 2020, Permeability Profiles Across the Crust-Mantle Sections in the Oman Drilling Project Inferred From Dry and Wet Resistivity Data: Journal of Geophysical Research: Solid Earth, **125**.

Khandelwal, M., and Ranjith, P.G., 2010, Correlating index properties of rocks with P-wave measurements: Journal of Applied Geophysics, **71**, 1–5.

Lai, J., Wang, G., Fan, Q. et al. Geophysical Well-Log Evaluation in the Era of Unconventional Hydrocarbon Resources: A Review on Current Status and Prospects: Surveys in Geophysics, **43**, 913–957

Liu, Q., Li, P., Jin, Z. et al., 2022, Organic-rich formation and hydrocarbon enrichment of lacustrine shale strata: A case study of Chang 7 Member: Science China Earth Sciences, **65**(1), 118–138.

Lu, M., Han, T., Wang, P., et al, 2023, Permeability of artificial sandstones identified by their dual-pore structure: Geophysical Journal International, **234**, 1422–1429.

Mavko, G., Mukerji, T., and Dvorkin, J., 2009, The rock physics handbook: tools for seismic analysis of porous media, Cambridge University Press.

Mulashani, A. K., Shen, C., Nkurlu, B. M., et al, 2022, Enhanced group method of data handling (gmdh) for permeability prediction based on the modified levenberg marquardt technique from well log data:

Energy, **239**, 121915.

Mavko, G. , and Nur, A., 1997, The effect of a percolation threshold in the kozeny-carman relation: Geophysics, **62**(5), 1480–1482.

Ngo, V. T., Lu, V. D., and Le, V. M., 2018, A comparison of permeability prediction methods using core analysis data for sandstone and carbonate reservoirs: Geomechanics & Geophysics for Geo Energy & Geo Resources, **4**, 129–139.

Prasad, M., 2003, Velocity-permeability relations within hydraulic units: Geophysics, **68**, 108–117.

Roberto, M., Dario, G., Luiz, E. S. V., et al., 2023, Iterative geostatistical seismic inversion with rock-physics constraints for permeability prediction: Geophysics, **88**(2), M105–M117.

Rezaee, M., Kadkhodaie-Ilkhchi, A., and Alizadeh, P.M., 2008, Intelligent approaches for the synthesis of petrophysical logs: Journal of Geophysics and Engineering, **5**, 12–26.

Shi, J., Zou, Y., Cai, Y., et al., 2021, Organic matter enrichment of the Chang 7 member in the Ordos Basin: Insights from chemometrics and element geochemistry: Marine and Petroleum Geology, **135**, 105404.

Slagle, A. L., and Goldberg, D. S., 2011, Evaluation of ocean crustal Sites 1256 and 504 for long-term CO2 sequestration. Geophysical research letters, **38**(16).

Timur, A., 1968, An investigation of permeability, porosity, and residual water saturation relationship for sandstone reservoirs: The Log Analyst, **9**, 8–17.

Tomski, J. R., Sen, M. K., Hess, T. E., et al., 2022, Unconventional reservoir characterization by seismic inversion and machine learning of the Bakken Formation: AAPG Bulletin, **106**(11), 2203–2223.

Walls, J., 1982, Effects of Pore Pressure, Confining Pressure, and Partial Saturation on Permeability of Sandstones, Ph.D. Thesis, Stanford University.

Walsh, J. B., 1965, The effect of cracks on the compressibility of rock: Journal of Geophysical Research, **70**(2), 381–389.

Watanabe, T., Makimura, M., Kaiwa, Y., et al, 2019, Elastic wave velocity and electrical conductivity in a brine-saturated rock and microstructure of pores: Earth Planets Space, **71**(1), 129.

Yang, H., Li, S. Y., Liu, X. Y., 2013, Characteristics and resource prospects of tight oil and shale oil in Ordos Basin: Acta Petrolei Sinica, **34**(01), 1–11.

Yasin, Q., Du, Q., Ismail, A., et al, 2019, A new integrated workflow for improving permeability estimation in a highly heterogeneous reservoir of Sawan Gas Field from well logs data: Geomechanics and Geophysics for Geo-Energy and Geo-Resources, **5**, 121–142.

Yang, Z., and Dong M., 2017, A new measurement method for radial permeability and porosity of shale: Petroleum Research, **2**(2), 178–185.

Yale, D., 1984, Network Modeling of Flow, Storage, and Deformation in Porous Rocks, Ph.D. Thesis, Stanford University.

Zhao, X. B., Chen, X. J., Huang, Q., et al, 2022, Logging-data-driven permeability prediction in low-permeable sandstones based on machine learning with pattern visualization: A case study in Wenchang A Sag, Pearl River Mouth Basin: Journal of Petroleum Science and Engineering, **214**, 110517.

Zhang, M., Dai, S., Pan, S., et al., 2023, Deciphering the laminated botryococcus-dominated shales in saline lacustrine basin, Western Qaidam Basin, NW China: Implications for shale oil potential: Marine and Petroleum Geology, **155**, 106397.

Zhao, W., Bian, C., and Li, Y., 2023, Enrichment factors of movable hydrocarbons in lacustrine shale oil and exploration potential of shale oil in Gulong Sag, Songliao Basin, NE China: Petroleum Exploration and Development, **50**(3), 520–533.

Zhang, G. Z., Chen, J. J., Chen, H. Z., et al., 2015, Prediction for in-situ formation stress of shale based on rock physics equivalent model: Chinese Journal of Geophysics, **58**(06), 2112–2122.

Zhang, L., Ba, J., Li, C., et al, 2022, Joint inversion of the unified pore geometry of tight sandstones based on elastic and electrical properties: Journal of Petroleum Science and Engineering, **219**, 111109.

Zhang, H., Zhao, B., Dong, S., et al., 2022, A Method for the Inversion of Reservoir Effective Permeability Based on Time-Lapse Resistivity Logging Data and Its Application: Geofluids, 1–13.

Zhang Lin received his Ph.D. degree in Exploration Geophysics from Hohai University in 2020, and is working as a lecturer in the School of Earth Sciences and Engineering, Hohai University, since 2020. His research interests are the elastic wave propagation theories of porous media and pore microstructure characterization.